FISEVIER

Contents lists available at ScienceDirect

Materials and Design

journal homepage: www.elsevier.com/locate/matdes



Additive manufacturing of biodegradable Zn-xWE43 porous scaffolds: Formation quality, microstructure and mechanical properties



Yu Qin ^{a,b}, Peng Wen ^{a,b,*}, Maximilian Voshage ^c, Yanzhe Chen ^{a,b}, Paul Georg Schückler ^c, Lucas Jauer ^d, Dandan Xia ^e, Hui Guo ^e, Yufeng Zheng ^e, Johannes Henrich Schleifenbaum ^{c,d}

- ^a The State Key Laboratory of Tribology, Tsinghua University, Beijing 100084, China
- ^b Department of Mechanical Engineering, Tsinghua University, Beijing 100084, China
- ^c Digital Additive Production (DAP), RWTH Aachen University, Steinbachstraße 15, 52074 Aachen, Germany
- ^d Fraunhofer Institute for Laser Technology, Steinbachstraße 15, 52074 Aachen, Germany
- ^e Department of Materials Science and Engineering, Peking University, Beijing 100871, China

HIGHLIGHTS

Novel Zn alloy porous scaffolds were fabricated by AM, which showed promising prospects for biodegradable applications

- The formation quality, microstructure and mechanical properties were investigated.
- Additive manufacturing of Zn—Mg alloy based powders showed promising prospects for biodegradable applications.

GRAPHICAL ABSTRACT



Additively manufactured Zn-xWE43 samples









ARTICLE INFO

Article history: Received 11 April 2019 Received in revised form 29 May 2019 Accepted 13 June 2019 Available online 15 June 2019

Keywords:
Additive manufacturing
WE43
Zn
Powder bed fusion
Porous scaffold

ABSTRACT

Zn is promising candidate material for biodegradable implants due to its acceptable biocompatibility and moderate degradation rate. However, the strength of pure Zn metal is regarded not enough. In this work, Zn-xWE43 porous scaffolds were fabricated by laser powder bed fusion (L-PBF) with different mass ratios of WE43: 2%, 5% and 8%. WE43 is a biodegradable Mg alloy with addition of Y and rare earth elements, and has been clinically verified. The formation quality, microstructure and mechanical properties were analyzed. L-PBF samples with high densification were achieved. Rapid cooling rate and the addition of WE43 together resulted to grain refinement. With increasing content of WE43, more Zn + Mg_2Zn_11 eutectics were precipitated, which increased tensile strength but decreased elongation. The formation of brittle MgZn_2 deteriorated strength in Zn-8WE43. Zn-5WE43 showed the highest tensile strength of 335.4 MPa, but the elongation was only 1%. The compressive strength and Young's modulus of Zn-5WE43 porous scaffolds was 73.2 MPa and 2480 MPa, while 22.9 MPa and 950 MPa for pure Zn porous scaffolds respectively. The present results addressed the key technical issues and pointed out the future directions on additive manufacturing of Zn alloy porous scaffolds for biodegradable application.

© 2019 The Authors. Published by Elsevier Ltd. This is an open access article under the CC BY-NC-ND license (http://creativecommons.org/licenses/by-nc-nd/4.0/).

^{*} Corresponding author at: Department of Mechanical Engineering, Tsinghua University, Beijing 100084, China. *E-mail address*: wenpeng@tsinghua.edu.cn (P. Wen).

1. Introduction

Each year, tens of millions of patients all over the world suffer from bone defects due to trauma, tumour resection, joint revision and other reasons. A large scale of bone defect makes it difficult for the bone to repair itself so that bone grafting is required. At present, bone defects are mainly filled and replaced with autogenous bones, allogeneic bone or artificial bone, and there are many problems such as limited sources and poor therapeutic effect [1]. Metals have been widely used in orthopedics since long before. There are four major challenges for the application of metals in bone grafting. Firstly, bones are in different shapes, requiring implants with customized geometry to bear load and transfer force smoothly; secondly, bone regeneration needs stress stimuli, requiring implants with the similar strength of bone to avoid stress shielding: thirdly, scaffolds with interconnected pores are necessary to provide space for ingrowth of bone cells; Finally the metal bone grafts are expected to be absorbed with osteogenic growth [2]. Plenty of research developments have been made on the four aspects [3–9].

Additive manufacturing, namely 3D printing, not only can efficiently and accurately achieve macro structures with customized shape, but also can produce micro structures like interconnected micro pores or different distribution of materials, by selectively melting/bonding discrete materials layer by layer in precision under computer control. It is regarded as an ideal method for tissue engineering and bio fabrication. Powder Bed Fusion (PBF) has become a successful additive manufacturing technology to manufacture non-degradable metal porous scaffolds like titanium alloys [3-5], CoCr alloys [6], and stainless steels [7], which fulfill the first three requirements for bone grafting as described above. However, non-degradable metal implants are lack of bioactivity and impede fully reconstruction of natural bones. Many hidden side effects may occur like infection and inflammation due to long term existence, especially for teenager patients whose bones are still growing. Second surgeries will cause serious physiological and economic burden to patients. Overall, additive manufacturing has been an ideal method to solve the first three challenges mentioned before.

Since the 21st century, biodegradable metals have attracted more and more attention in the research field of biomaterials and medical science. A variety of new biodegradable alloys based on Mg, Fe and Zn have been developed in order to meet the requirements of an ideal biodegradable implant: good biocompatibility, suitable biodegradation rate and enough mechanical properties [8,9]. Biodegradable Mg alloys have been studied most intensively. Mg alloys like WE43 have realized a small scale of clinic applications including vascular stents and bone fixture devices [10]. However, Mg degrades too fast with the formation of hydrogen and a local increase of PH value. Fe degrades too slowly with the formation of iron oxides which are difficult to decompose. The degradation rate of Zn is intermediate between Mg and Fe. Zn is an essential nutrient element in human body. The degradation products of Zn are also biocompatible, and no hydrogen is given off. Zn based metals have become a promising structural material for biodegradable implants [11-17]. Meanwhile, as an attractive fabrication technology, additive manufacturing has been tried on pure Zn metal and Zn alloys [18-23]. Many novel biodegradable alloys have been developed, and some of them have realized clinical applications. However, development on additively manufactured biodegradable metals is still limited [24].

The melting point and boiling point of Zn is only 420 and 907 °C respectively. Massive evaporation occurs when Zn is melted by a high energy beam in PBF process. Electron beam is not suitable to melt Zn since evaporation products obstruct the propagation of electron beam in the vacuum. Laser powder bed fusion (L-PBF) is the most promising method for additive manufacturing of Zn based metal porous scaffolds. Montani et al. [18] published the first peer-reviewed paper on L-PBF of pure Zn metal in 2017. The highest relative density of L-PBF bulk samples was only 88%. Severe evaporation fume and spatter were observed during L-PBF process. The evaporation fume contained a large amount of

small particles that scattered laser beam, making the laser energy input unstable on powder bed and causing porosity inside the samples.

To solve this problem, Wen et al. [19] introduced a customized gas circulation system, and systematically studied the effect of processing parameter on densification by response surface methodology. After processing optimization, the relative density of pure Zn L-PBF bulk samples was above 99.5% stably in a wide processing window. The hardness, yield strength, ultimate strength and elongation of pure Zn L-PBF bulk samples were 42 HV, 114 MPa, 134 MPa and 10.1% respectively [20]. L-PBF samples showed higher hardness and tensile strength compared with casting, rolling and extrusion, which was attributed to grain refinement. The tensile strength of Ti6Al4V, a widely used medical metal in orthopedics, is around 1000 MPa as bulk metal [3]. Therefore the mechanical strength of pure Zn is regarded not enough as the material of orthopedic application.

There have been many reports on the improvement of mechanical properties of Zn based metals by alloying with biocompatible elements like Mg, Ca, Sr, Ag, etc. [14]. They are bulk samples obtained by conventional manufacturing methods. Very limited reports have tried on L-PBF of Zn alloy powders. Shuai et al. studied microstructure and mechanical properties of Zn-xMg (x = 0, 1, 2, 3, 4 wt%) [21] and Zn-xAg (x = 0, 2, 4, 6, 8 wt%) bulk samples by L-PBF [22]. They found that the optimized mechanical properties were obtained with Zn-3 Mg and Zn—6Ag. The tensile strength and elongation was measured respectively as 61.3 MPa and 1.7% for pure Zn; 222.3 MPa and 7.2% for Zn-3 Mg; 293 MPa and no data of elongation for Zn—6Ag. The mechanical properties of Zn alloyed samples increased much compared with those of pure Zn samples. No data has been found on the mechanical performance of additively manufactured porous scaffold of Zn and its alloys.

WE43, a type of biodegradable Mg alloy, has been clinically verified in Europe [25]. It is expected that alloying with WE43, can not only improve the strength of pure Zn with the help of elements like Mg and RE, but also can guarantee biocompatibility. In this research, Mg alloy powder WE43 was mixed with pure Zn powder to form Zn-xWE43 (x = 0, 2, 5, 8, wt%) alloy powders, which were used to fabricate bulk samples and porous scaffolds by L-PBF. The influence of WE43 content on formation quality, microstructure and mechanical properties was clarified.

2. Materials and methods

2.1. Materials

Nitrogen atomized pure Zn powder was supplied by NANOVAL (Berlin, Germany). The mean powder size d_{50} was 28.2 μ m at the range + 15/-45 µm. Gas atomized WE43 powder was provided by Materials Science and Engineering Werkstoffzentrum Clausthal UG (Clausthal, Germany). Besides Mg, WE43 powder contained 3.48%Y, 1.6% Nd, 0.7% Gd and 0.4% Zr in mass ratio. The WE43 powder was sieved to the range from 25 to 63 μm. More detailed information on the two powders can refer to our previous works [19,26]. Different amounts of WE43 powder was added into pure Zn powder to form Zn-xWE43 (x = 2, 5, 8, wt%) alloyed powder, which was thoroughly mixed by mechanical vibration in a closed cylinder with shielding argon gas. Fig. 1 shows the morphology of used powders by scanning electron microscope (SEM). Pure Zn powder was in spherical and uniform shape. For WE43 powder, both spherical and elongated particles were observed. Some small particles (<10 µm) adhered to the surface of large particles. The mixed powder was immediately used after vibration to avoid separation due to the difference of density of the two component powders. Pure Zn metal plate with 25 mm thickness was used as the substrate during L-PBF process.

2.2. L-PBF process

A compact L-PBF machine (ACONITY, Germany) was used. The optical system consists of a single mode ytterbium fiber laser (IPG YLR-400)

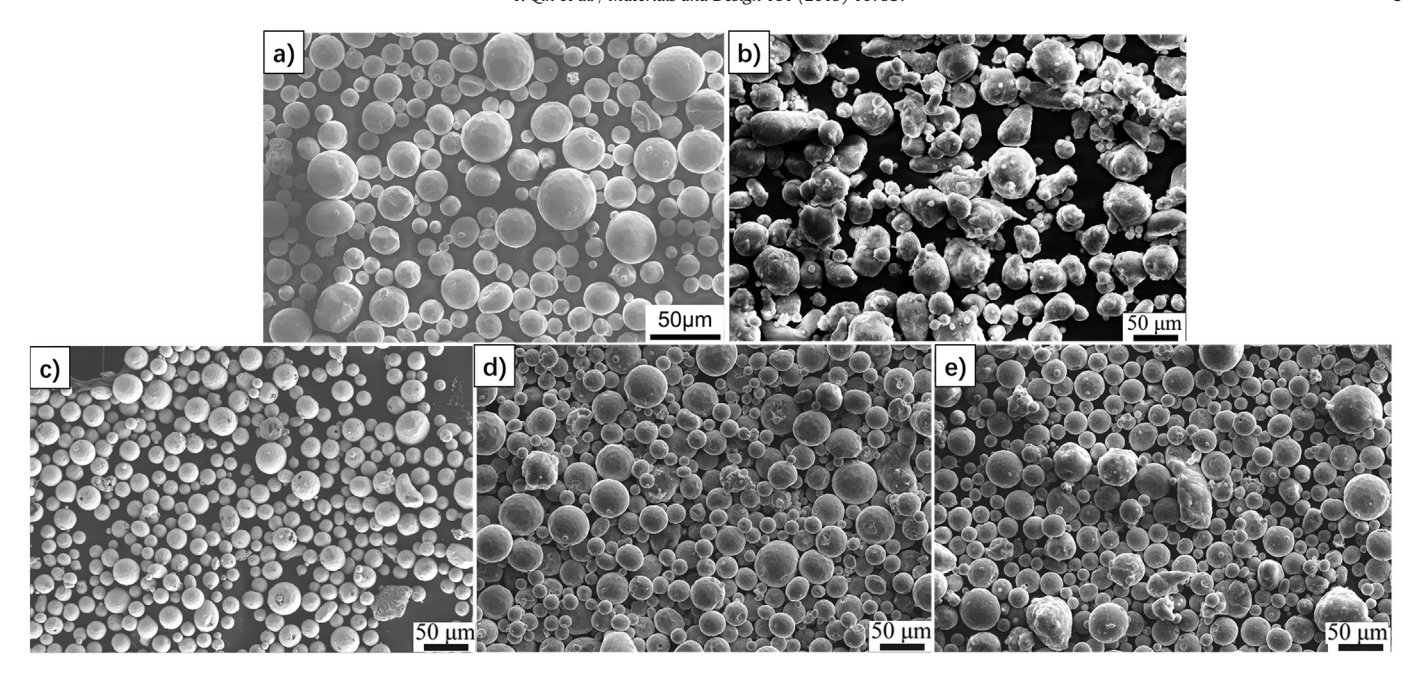


Fig. 1. Morphology of powders: a) pure Zn, b) WE43, c) Zn-2WE43, d) Zn-5WE43, e) Zn-8WE43.

with the laser spot diameter of 75 µm and the maximum power of 400~W at wavelength of $1070~\mu m$, a galvanometric scanner (SCANLAB hurry SCAN 20) and a f-theta focusing lens (SILL S4LFT 3254/126). Considering enormous evaporation and high chemical activity during laser melting of Zn and Mg, a specially designed gas circulation system was used with two main purposes: to keep the process from oxidation and other harmful gas intrusion, and to eliminate the negative effect of evaporation on the processing stability. The key parameters in L-PBF process include laser power P, scanning speed V, hatch spacing Hs, and layer thickness Ds, which together determine the input of laser energy $Ev = P / (V \cdot Hs \cdot Ds)$ [27]. Preliminary results showed that samples were obtained with good formation quality by setting parameters as: $P = 70 \text{ W}, V = 500 \text{ mm/s}, Hs = 70 \text{ }\mu\text{m}, Ds = 30 \text{ }\mu\text{m} \text{ and } Ev = 100 \text{ }\mu\text{m}$ 66.7 J/mm³ for pure Zn powders, which was used for all the ZnxWE43 samples in this research. The focal plane of laser was set on the top layer of powder bed. A zig-zag exposure pattern with a 90°

rotation per layer was used for bulk samples. More details about the equipment and the effect of processing parameters on formation quality can refer to our previous work on L-PBF of pure Zn [19,23].

Both pure Zn and Zn-xWE43 powders were used to make three types of structures by L-PBF. Solid cubes of 5 * 5 * 10 mm³ were built to investigate densification and microstructures. Solid slabs of $10\times 2\times 50~\text{mm}^3$ were built to make tensile specimens, which was cut into ASTM 8E standard shape and size later by wire-electrode cutting as Fig. 2a and b shows. The tensile direction was parallel along with the building direction. Three duplicable samples were tested to get the average value and the standard deviation. Porous scaffolds in cylinder shape with diamond lattices were built, which was just the same as reference [28] in order to make a better comparison. A cylindrical strut of 400 μm in diameter and a pore size of 600 μm in diameter were used. The diameter of the cylinder was 10 mm with a height of 60 mm. The designed structural porosity was about 67% with interconnected

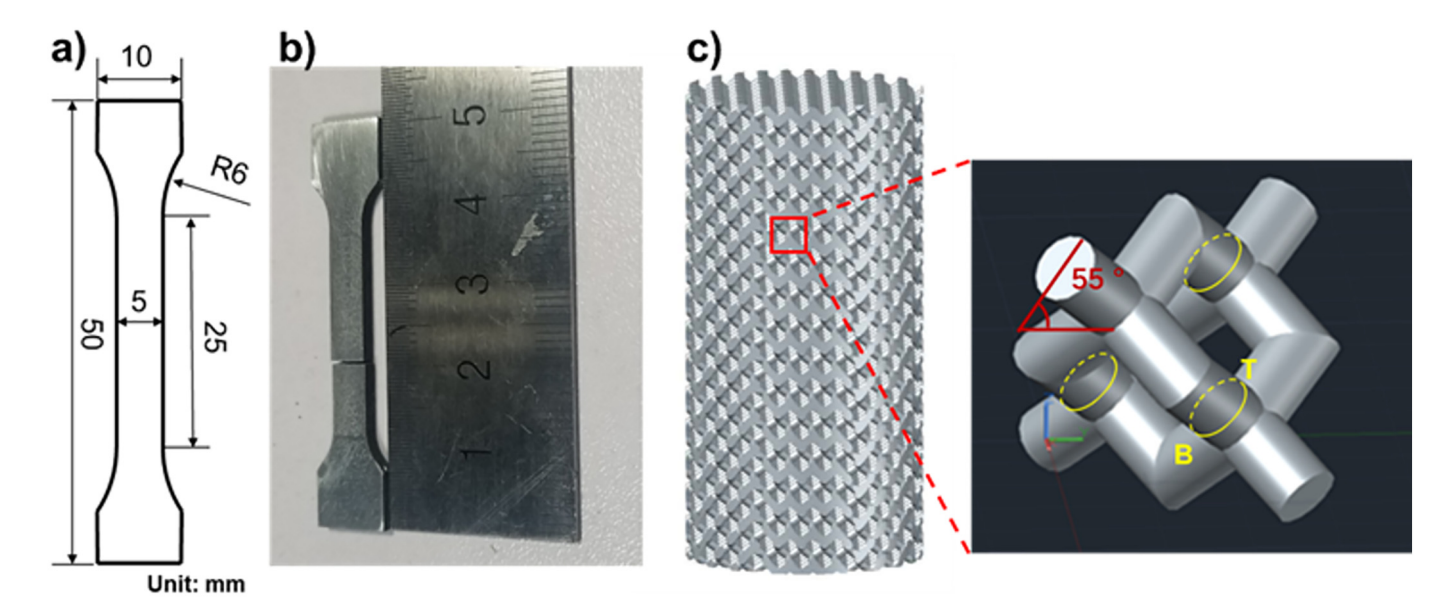


Fig. 2. Illustration of L-PBF samples: dimensional size a) and picture b) of tensile samples, c) shape of porous scaffolds.

pores. For the struts of porous scaffolds, zig-zag plus outline contouring exposure pattern was used. The number of exposure tracks was very limited at the cross section of struts if only zig-zag hatching was used [20]. Bottom (B) and top (T) side of a strut was labeled as Fig. 2c shows, which was used to indicate the influence of overhang on formation quality.

2.3. Formation quality and microstructure characterization

Two categories of porosities (or densities) are often mentioned for porous scaffolds. One category refers to interconnected cavities resulted by geometrical design, so called geometrical porosity, which are fabricated purposely with certain shape and amount. They are necessary to provide space for the growth of cells and tissues into scaffolds in order to form a reliable bonding between scaffolds and human bones. Normally, an increase in geometrical porosity improves biological performance, but deteriorates mechanical performance [2]. The other category indicates closed pores at the cross section of struts resulted by improper processing conditions, so called processing porosity. Processing porosity needs to be inhibited as far as possible, since it deteriorates the mechanical performance of scaffolds unexpectedly. Densification means the prevention of processing porosity, and is the most significant indicator of formation quality for L-PBF process.

Processing porosity was tested with image analysis of cross sections, which was much accurate for samples with high density according to Spierings et al. [29]. The cross section parallel to building direction was cut and polished. Optical microscopy images of the entire cross section were observed, and 5 different regions of 2.2 * 1.7 mm² (A_{total}) were picked up randomly. The total area of pores (Apore) was measured for each region under a $50 \times$ objective lens. The porosity was calculated as A_{pore}/A_{total}, while the processing relative density was 1- A_{pore}/A_{total}. For geometrical porosity of porous scaffolds, it was 1-m_{sca}/m_{vol}. The mass of porous scaffolds was measured by after ultrasonic cleaning and indicated as m_{sca}. The value of m_{vol} was calculated by the outline dimensional size of porous scaffolds assuming that no pore exists inside. Microstructure of L-PBF samples were characterized using scanning electron microscope (SEM) after polishing and etching with 2 vol% hydrogen nitrate for 10 s. Energy dispersive x-ray spectroscopy (EDX) was applied to analyze chemical composition. Phase identification was conducted by X-ray diffraction (XRD) at 40 kV and 150 mA, using a continuous scan mode. A quick scan at 4°/min was conducted over a range of $2\theta = 10-90^{\circ}$ to give a general overview of the diffraction peaks.

2.4. Mechanical property test

Vickers hardness of L-PBF samples was measured with a load of 300 g. Ten measurements were made along the axis of the build direction at the center of the bulk samples. Tensile test was conducted at room temperature by a dynamic thermal-mechanical tester (Gleeble 1500D, USA) at a speed of 1.5 mm/min. The tensile fracture surfaces

were observed by SEM. Porous scaffolds were cut to 20 mm in length by wire-electrode cutting, and were compressed at room temperature by a modified hydraulic press machine (RDF, China) at the speed of 4.5 mm/min. A high speed camera recorded the process of compressive test. For each tensile and compressive condition, three samples were tested to get the average value and the standard deviation.

3. Results and discussion

3.1. Formation quality

Fig. 3a shows the image of as-built samples on the substrate after L-PBF process. Fig. 3b–d show typical images of cross-sections of L-PBF bulk samples. The relative density of Zn-xWE43 (x=2,5,8) was $99.93\pm0.04\%$, $99.75\pm0.10\%$, and $99.47\pm0.15\%$ respectively. Very few pores were found on Zn-2WE43 samples, which was similar to pure Zn bulk samples. The relative density of pure Zn samples was over 99.9% under the same processing condition [19]. With increasing content of WE43, the processing porosity increased at the cross section. Some fine separated spherical pores were observed at the cross section of Zn-5WE43 and Zn-8WE43 bulk samples. Most of them distributed randomly at the whole cross section, and there was a bit high concentration of pores at the edge. Zn-8WE43 shows the highest processing porosity, and the edge of samples showed slightly rugged lines, indicating a relatively poor surface quality.

Fig. 4 shows the enlarged pictures of porous scaffolds after L-PBF process. A large amount of powders adhered to struts, resulting in a high surface roughness and a thicker strut than the design. Not much difference was found on surface quality of different Zn-xWE43 porous scaffolds as shown in Fig. 4b-e. The average diameter of struts was 562 μm in the range of 500–600 μm , much bigger than the design value 400 μm . Accordingly, the obtained geometrical porosity was 45 \pm 1.8%, much lower than the design value 67%. There was a huge geometrical error between the L-PBF porous scaffolds and the design.

3.2. Microstructure

As Fig. 5 shows, strong diffraction peaks corresponding to hcp-Zn were detected in all Zn-xWE43 samples. For pure Zn, no secondary peak of zinc oxides was found in the XRD profiles, meaning no oxidation appeared during L-PBF process. With increasing the content of WE43, microstructure of Zn-xWE43 samples became more complicated with precipitated intermetallic compounds. For Zn-2WE43, the curve was very similar to that of pure Zn [20], and only a few minor signals were detected in correspondence with intermetallic Mg_2Zn_{11} . For Zn-5WE43 and Zn-8WE43, intermetallic compounds Mg_2Zn_{11} and $MgZn_2$ were both detected clearly. The signal intensity of Mg_2Zn_{11} and $MgZn_2$ in Zn-5WE43 dropped much compared with that in Zn-8WE43, indicating the different content of intermetallic compounds. In addition, ambiguous phases were found at $2\theta = 74$ and 78° for Zn-5WE43 and Zn-

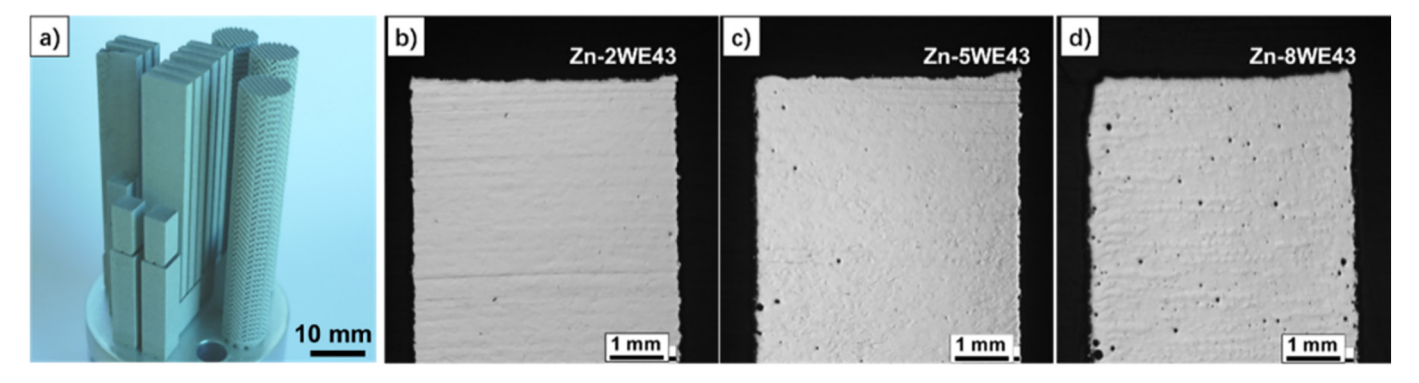


Fig. 3. Picture of L-PBF samples: a) as-built samples on the substrate, b-d) cross sections of Zn-xWE43 bulk samples, building direction: from bottom to top.

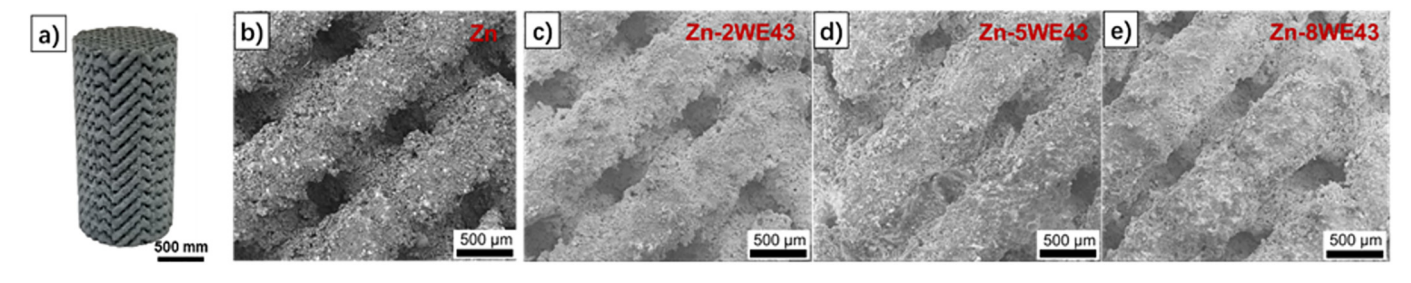


Fig. 4. Porous scaffolds made by L-PBF: a) macro image, b-e) enlarged parts of Zn-xWE43.

8WE43. Possibly they were YZn_5 and NdZn, which requires further confirmation.

Fig. 6 shows microstructures of Zn-xWE43 samples under SEM observation. Two regions of different microstructure were observed in Fig. 6a for Zn-2WE43. It indicated that the chemical composition distribution inside the L-PBF samples was not homogeneous, which was regarded as the result of mechanically mixed powders. The bottom side was mostly made up of pure Zn, where α -Zn grains were found. Much finer α -Zn grains plus precipitated phases were observed at the top side. As the enlarge image in Fig. 6b shows, some eutectic phase precipitated at the grain boundary of α -Zn grains. According to XRD and EDX analysis, it was α -Zn + Mg₂Zn₁₁ eutectic structure, which precipitated at 364 °C according to the Zn—Mg binary phase diagram [33]. Zn-5WE43 showed two types of different microstructure in different regions. Fig. 6c shows the typical microstructure of Zn-5WE43. Fine α -Zn plus Mg₂Zn₁₁ eutectic precipitates occupied the majority, leaving a small amount of local α-Zn bulks. MgZn₂ was also observed in Zn-5WE43 in some regions as Fig. 6d shows, which also indicated the inhomogeneous distribution of chemical compositions in mixed powders.

With increasing the content of WE43 in the mixed powder, the microstructure of L-PBF samples became more homogenized. Homogenous microstructure was observed in Zn-8WE43 samples, and very few local α -Zn bulks were observed. As Fig. 6e shows, α -Zn, Mg_2Zn_{11} and $MgZn_2$ were all clearly observed, which was consistent with XRD analysis results. $MgZn_2$ appeared in large number with polygonal shape. The element ratio at typical positions was measured by EDX and listed in Fig. 6f. Only very few Mg was detected in α -Zn grains since the solid solubility of Mg in α -Zn is quite low according to Zn—Mg phase diagram. The measured content of Mg increased to about 3% in α -Zn + Mg_2Zn_{11} and to about 7% in MgZn_2, which showed good agreement between the compositional ratio and the observed morphology of the different microstructures.

As the content of WE43 increased from 2% to 5%, the grain size of α -Zn decreased from 2 μ m to below 0.5 μ m. The grain size of L-PBF produced pure Zn samples was about 5.6 μ m under the same processing

condition [19]. The addition of WE43 tremendously refined the grain size. When WE43 was further increased to 8%, it was difficult to find $\alpha\text{-}Zn$ grains in the samples, and the majority of microstructure was MgZn $_2$ with very small size of about 0.5 μm at the matrix of $\alpha\text{-}Zn$ + Mg $_2Zn_{11}$ eutectic structure.

3.3. Mechanical properties

Fig. 7 shows the hardness and tensile properties of L-PBF bulk samples. The measurement data of pure Zn was referred from our previous work [20], which was used for comparison. The hardness of Zn-xWE43 (x = 0, 2.5 and 8) samples was measured as 42 ± 3 [20], 114 ± 13 , 146 \pm 14, 169 \pm 8 HV respectively. With increasing WE43 content, the hardness of L-PBF samples substantially increased. Although inhomogeneous microstructure was observed in Zn-2WE3, no significant difference of hardness was found among all the measurement positions for all Zn-xWE43 samples. The yield and tensile strength of pure Zn samples was 114 and 134 MPa in average [20]. With the addition of 2%and 5% WE43, it increased to 298.5 \pm 12 and 335.4 \pm 10 MPa respectively. With further increasing WE43 addition to 8%, the average tensile strength dropped to 154.1 \pm 16 MPa. The elongation after break was 10.1 \pm 1.2 [20], 1.8 \pm 0.1, 1 \pm 0.1, 0.9 \pm 0.1%, respectively for ZnxWE43 (x = 0, 2, 5 and 8). With increasing the content of WE43, the ductility decreased to a very low level.

The fracture surfaces of Zn-xWE43 (x=2,5 and 8) samples are shown in Fig. 8. Brittle fracture was observed with flat surfaces for all the samples. The fracture surface of Zn-2WE43 was slightly rougher than that of Zn-5WE43 and Zn-8WE43, indicating a little higher value of elongation. Compared with a few of dimples shown at the fracture surface of pure Zn samples [20], almost no indication of ductile deformation was found with the addition of WE43. Microscopically, there were mainly cleavage steps and cleavage planes surrounded by tearing ridges at the fracture surfaces, which indicated a cleavage fracture mode. The size of cleavage planes of Zn-2WE43 was significantly larger than that of Zn-5WE43 and Zn-8WE43 samples, which corresponded to

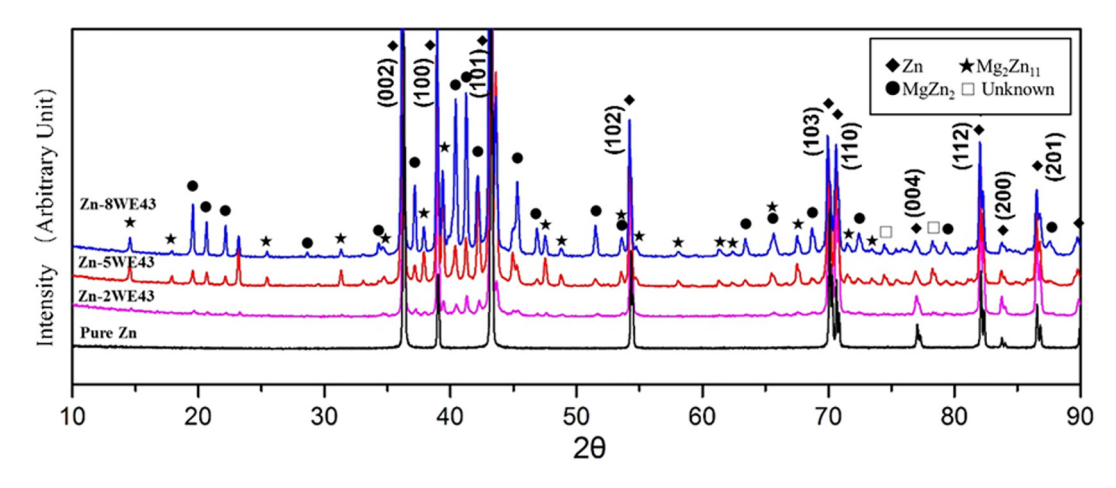


Fig. 5. X-ray diffraction pattern of Zn-xWE43 L-PBF samples.

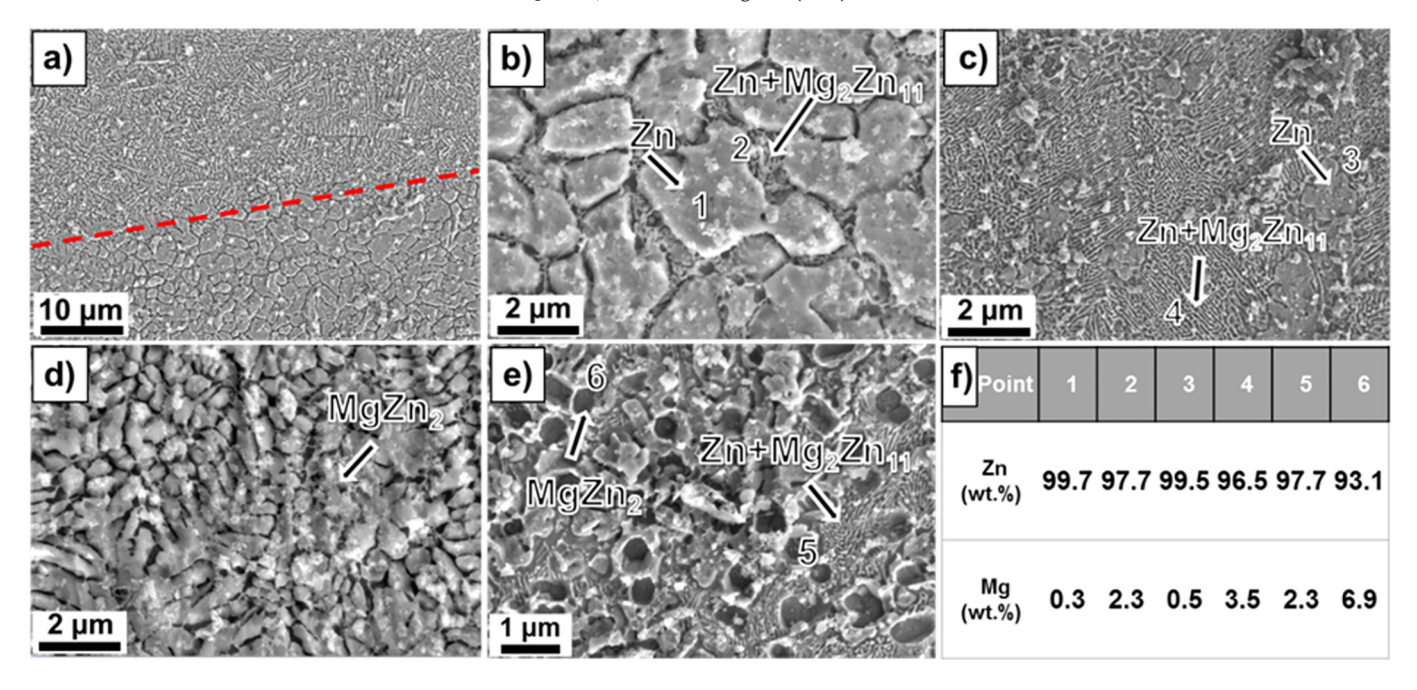


Fig. 6. Microstructure analysis: a, b) Zn-2WE43, c, d) Zn-5WE43, e) Zn-8WE43, f) element ratio by EDX analysis.

their different grain size. Moreover, many spherical pores were found at the fracture surface of Zn-8WE43 samples. No stretching was observed around pores after the fracture, which indicated that the drop of strength was mainly determined by the massive formation of brittle intermetallic eutectics.

Fig. 9 shows the compressive properties of Zn-xWE43 porous scaffolds including pure Zn. There was a stable compression plateau after yielding in the compression curve of pure Zn porous scaffolds. The final increase in the stress curve indicated high formation quality of the struts of porous scaffolds, which was resulted from high densification due to an appropriated processing control. With regard to Zn-2WE43 samples, the stress curve started with a linear elastic region, then its slope rapidly decreased, followed by a plateau stage with fluctuation, and finally a dense compression state occurred, which was much

like that of pure Zn porous scaffolds. For Zn-5WE43 and Zn-8WE43 porous scaffolds, they were destroyed the linear stage, namely high brittleness. Fig. 10 shows pictures of porous scaffolds after compression with different addition of WE43. Pure Zn and Zn-2WE43 showed massive plastic deformation before fracture as shown in Fig. 10a and b. Zn-5WE43 and Zn-8WE43 all showed great brittleness with a flat fracture surface. The angle of the fracture surface was both 55° to the horizontal plane as shown in Fig. 10c and d. For Zn-2WE43, a bevel deformation with an angle of 55° was also observed during the compressive test as shown in Fig. 2b after 20% deformation. The Video 1 of deformation process are available in the supplementary data. For pure Zn, the deformation process of porous scaffolds was just like that of solid ductile metal parts, which showed a typical shape of drum during deformation as shown in Fig. 2a after 20% deformation.

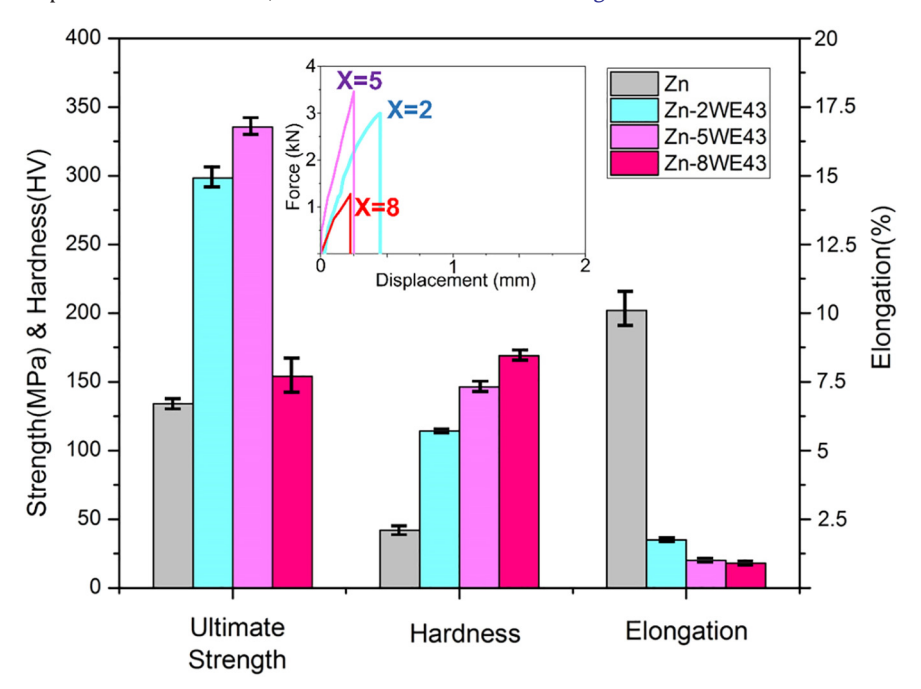


Fig. 7. Tensile properties and hardness of Zn-xWE43 L-PBF bulk samples.

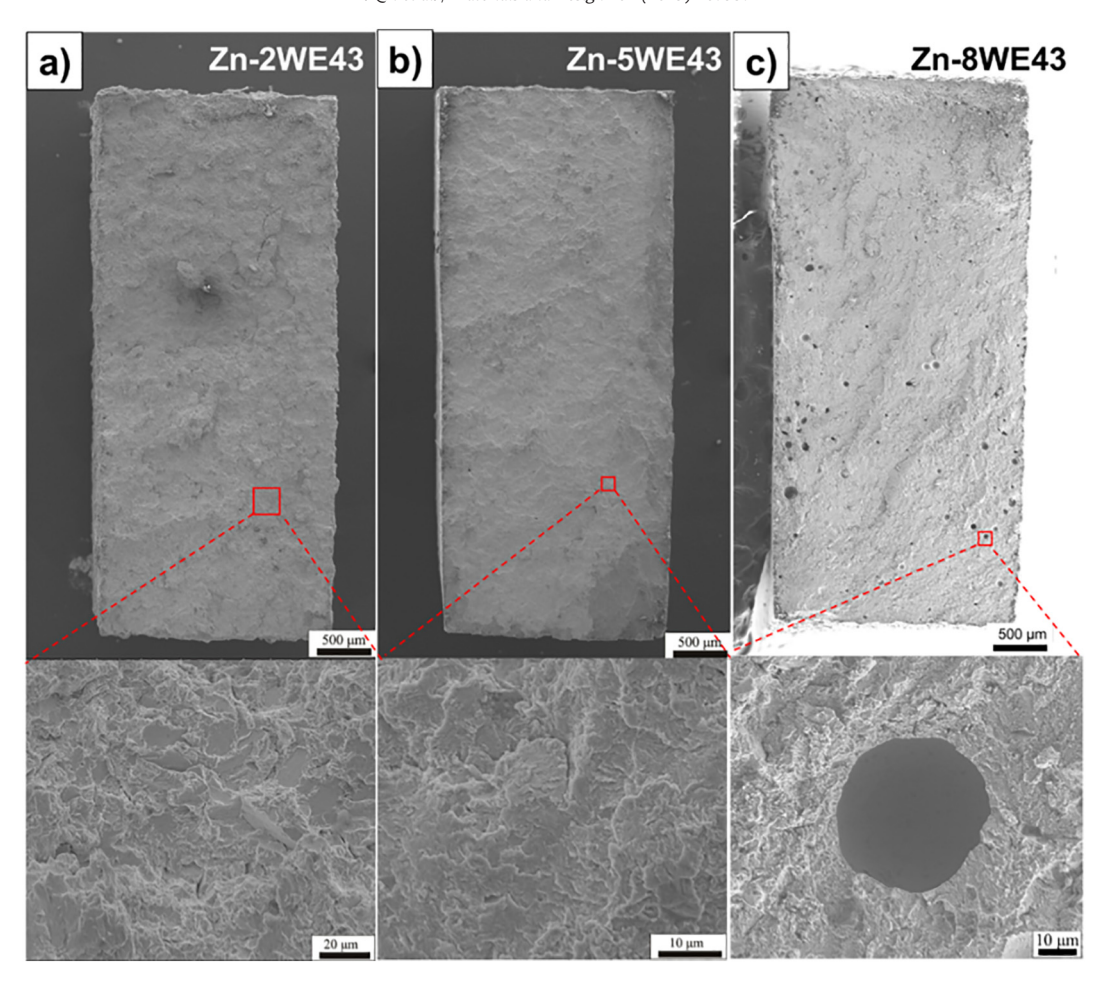


Fig. 8. Tensile fracture surface of Zn-xWE43 bulk samples: a) Zn-2WE43, b) Zn-5WE43, c) Zn-8WE43.

Fig.10e shows the enlarged fracture surface of Zn-8WE43 porous scaffold. Very smooth fracture surface was observed like tensile fracture surface. Several minor pores were also found at the cross section of

some struts. The yellow circles inside the picture show the designed diameter of struts, which are also illustrated in Fig. 2b. A lot of partially melted powder attached to the surface of solidified struts, which caused

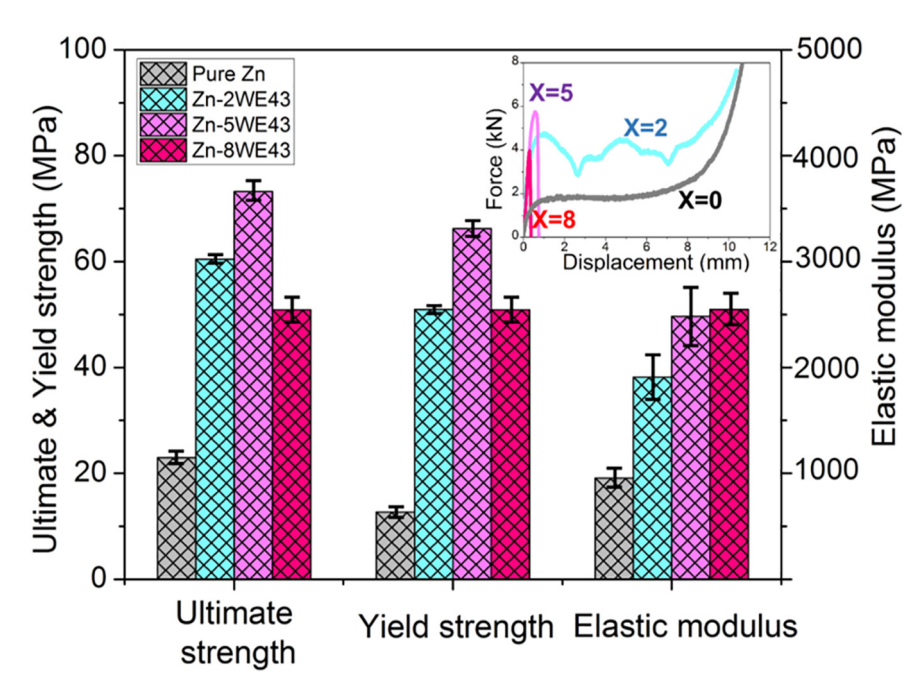


Fig. 9. Compression properties and curves of Zn-xWE43 porous scaffolds.

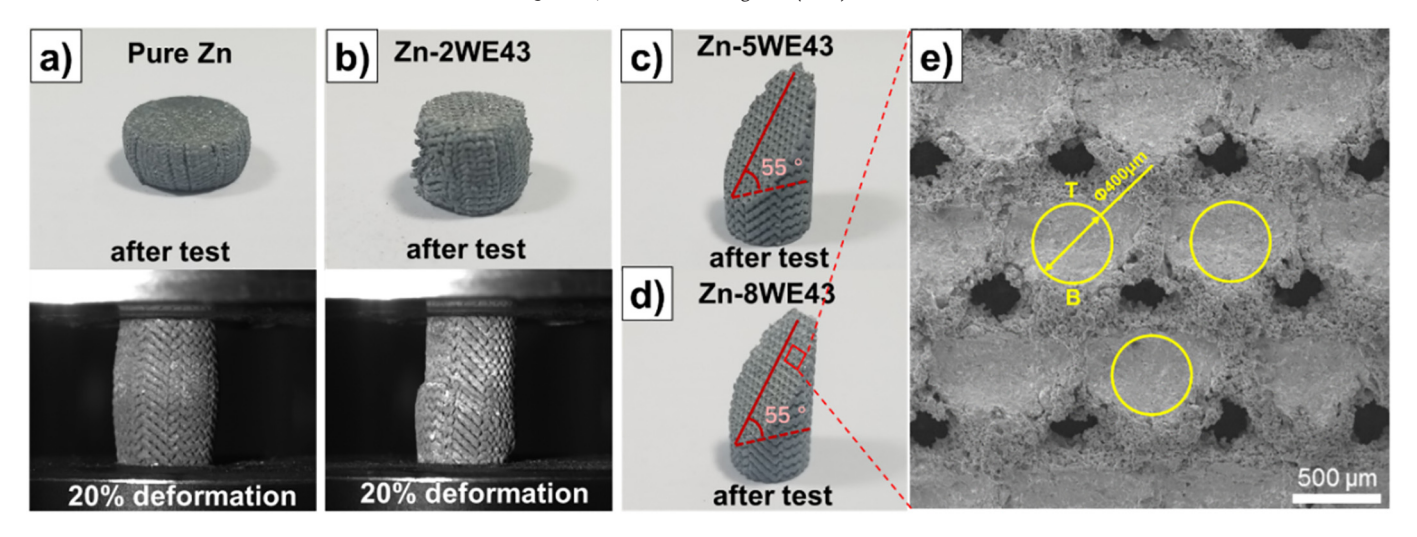


Fig. 10. Porous scaffolds during and after compression test a-d), enlarged picture of Zn-8WE43 fracture surface.

the geometrical error between design and L-PBF porous scaffolds. The letter T and D respectively mean the top side and bottom side of the struts. It can be found that much more powder attached to the bottom of struts. The attached powder didn't contribute to strength since they were loosely connected. The average compressive strength was 22.9 \pm 1.7, 60.5 \pm 1.1, 73.2 \pm 2.6, 50.9 \pm 3.1 MPa, the yield strength was 12.7 \pm 1.5, 50.9 \pm 1.0, 66.2 \pm 2.4, 50.9 \pm 3.1 MPa, and the elastic modulus was 950 \pm 114, 1910 \pm 257, 2480 \pm 270, 2540 \pm 203 MPa, respectively with the addition of WE43 as 0, 2, 5 and 8%. The change of compressive strength of porous scaffolds was consistent with tensile strengths of bulk samples. The strength increased with the addition of 2 and 5% WE43, and decreased with the addition of 8% WE43 compared with pure Zn.

3.4. Discussion

The melting point and boiling point of Zn and Mg are both very low: 420/907 and 650/1091 °C respectively. Massive evaporation was observed during L-PBF of pure Zn and Mg alloy powders [18,26]. It is the key issue to eliminate the side effect of evaporation in order to achieve good formation quality during L-PBF of Zn and Mg based metals. With a customized gas circulation system and optimized laser energy input, the negative effect of evaporation was eliminated, and L-PBF produced samples with good formation quality were obtained for pure Zn samples [19]. With the same gas circulation and laser energy input optimized for pure Zn powder, the relative density of Zn-xWE43 bulk samples reached over 99.47%. Zn-8WE43 showed the highest processing porosity among the used samples.

According to a report of L-PBF of ZK60 [31], the mass ratio of Zn element decreased from 5.22% in the powder to 4.41% in the as-built sample due to the burning loss resulted by evaporation; while the content of Mg rose from 94.05% to 94.45%. It is direct evidence that the evaporation tendency of Zn was greater than that of Mg during laser melting. Moreover, the oxidation tendency of Mg is much higher than that of Zn. For L-PBF of Mg alloy powders, higher laser energy input is needed to melt Mg oxide film. The optimal laser energy input for L-PBF of WE43 powder was reported as $P=200~\rm W,~V=700~mm/s,~Hs=40~\mu m,~Ds=30~\mu m$ [23]. After calculation, the specific laser energy density Ev was 238.1 J/mm³ for WE43 powder, larger than 66.7 J/mm³ used in this research. Therefore, with increasing Mg content in the Zn based alloy powder, the optimal processing parameters need to be adjusted considering the effect of Mg on evaporation and melting.

There was a big difference between the designed geometrical porosity 67% and the obtained value 45% for porous scaffolds. As Fig. 4 shows,

the diameter of the obtained struts of porous scaffolds was much larger than the design value. The surface tension and viscosity of pure Zn in molten state is about 782 mN/m and 3.85 mPa·s, respectively. The fluidity and the wetting of molten Zn are both very good. Molten Zn easily takes a capillary action among powders and sinters the surrounding powders together [23]. Therefore, a lot of powders attached to the molten pool, which increase the strut diameter compared with design value. As Fig. 10e shows, the interior part within the design diameter was almost dense, while the outer ring was loose sintered powders. Meanwhile, the overhang angle of strut was 35° according to design as shown in Fig. 2. The amount of attached powder was more at the bottom (B) side than that at the top (T) side of a strut, which is a typical overhang phenomenon well reported in L-PBF process. The effect of overhang angle on formation quality is different for different powders. For example, a literature reported that the favorable overhang angle should be over than 30, 40 and 45° respectively for Ti6Al4V, AlSi12 and stainless steels [32]. So far, no report has been found on the effect of overhang angle on L-PBF of Zn and Mg based metals.

Prosek et al. [30] studied microstructure of casted Zn-xMg alloys. Zn-3 Mg consisted of α -Zn + Mg₂Zn₁₁ eutectic entirely. Zn-4 Mg consisted of 71% α -Zn + Mg₂Zn₁₁ eutectic and 29% MgZn₂. In this research, with different content of WE43, microstructure in Zn-xWE43 samples was significantly different. In the case of Zn-2WE43, the major phase was α -Zn, and only a small amount of α -Zn + Mg₂Zn₁₁ eutectic was observed at grain boundary due to the peritectic reaction: $L + MgZn_2 =$ Mg_2Zn_{11} [30]. For Zn-5WE43, α -Zn + Mg_2Zn_{11} eutectic was dominant with a small amount of α -Zn and MgZn₂. For Zn-8WE43, the microstructure was mainly made up of MgZn₂ at the matrix of α -Zn + Mg₂Zn₁₁ eutectic. However, L-PBF produced Zn-5WE43 samples contained much less MgZn₂ than as-cast Zn-4 Mg did. The existence of α -Zn phase was still observed. The reduction of precipitated phase in L-PBF samples was mainly caused by the fast cooling rate. The increase in Mg content led to grain refinement due to the precipitation of α -Zn + Mg₂Zn₁₁ eutectic [33]. The grain size of Zn-1 Mg alloy was about 50 μm for extrusion [34] and 20 μm for casting samples [33]. Yang et al. [21] reported grain size of L-PBF produced Zn-2 Mg alloy as 6.7 μm, since the cooling rate of L-PBF was faster than that in extrusion and casting. The L-PBF produced Zn-2WE43 samples had much finer grain size, about 2 μm in this research. The grain size was <0.5 μm for the polygon MgZn₂ in L-PBF produced Zn-5WE43 and Zn-8WE43. The addition of rare earth elements in WE43 powder induced a strong effect of grain refinement as well [35]. Mechanical mixing of two separate powders by vibration is convenient to adjust the content of alloying element, but is difficult to get homogenous distribution of chemical composition

and microstructure in L-PBF samples. With the obtained knowledge, more work need to be done with alloy powders made by melting and atomization.

Hardness increased with increasing the content of WE43. The hardness of L-PBF pure Zn samples was 42 HV, much higher than casting and extrusion samples due to grain refinement effect [19]. The hardness increased from 114 HV in Zn-2WE43 to 146 HV in Zn-5WE43 samples due to increase of α -Zn + Mg₂Zn₁₁ eutectic. The hardness of Zn-8WE43 was further increased, which was attributed to the formation of MgZn₂. Mostaed et al. [34] studied the mechanical properties of extruded ZnxMg with Mg content from 0.15% to 3%. Entirely $Zn + Mg_2Zn_{11}$ eutectic was found in Zn-3 Mg, which showed he highest tensile strength of 400 MPa and very low elongation of 0.8%. The $Zn + Mg_2Zn_{11}$ eutectics increased the strength and decreased the ductility. Vojtech et al. [33] studied casted Zn-xMg (x = 1, 2 and 3 wt%). Zn-3 Mg casted samples were nearly made up of all the $Zn + Mg_2Zn_{11}$ eutectics as well. However, the tensile strength of Zn-3 Mg decreased to <40 MPa compared with 150 MPa of Zn-1 Mg casted samples. Yang et al. [21] studied the mechanical properties of Zn-xMg (x = 1, 2, 3 and 4 wt%) by L-PBF process. They found that the highest tensile strength and the hightest elongation reached together in Zn-3 Mg samples, which were 222 MPa and 7.2% respectively. Further increasing Mg content to 4%, both strength and elongation rate decreased to 166 MPa and 3.1%, which was explained by the formation of MgZn₂. In this research, tensile strength firstly increased and then decreased with increasing the content of WE43. Zn-5 Mg showed the highest strength of 335.4 MPa, which are higher than the values of other fabrication methods. The elongation decreased with increasing content of WE43. The highest elongation was 10.1% for pure Zn bulk samples. On one hand, grain refinement brings strengthening effect according to Hall-Petch Equation. For L-PBF samples with high densification, the strength usually is higher or equivalent compared with casted and plastic deformed samples; the elongation is higher than casted samples and lower than plastic deformed samples [20,36]. On the other hand, the change of phase component hugely affects mechanical properties.

According to the published results, it clearly shows that different processing methods also have a great impact on mechanical behavior of Zn alloys [14]. Besides, it also should be pointed out that the effect of formation quality on mechanical properties has been ignored in many published results. The additively manufactured samples were obtained by numerous melting and solidification, Stable formation quality is hard to realize especially for processing Zn and Mg metals which show high evaporation and oxidation tendency. Formation quality, as well as the geometrical error mentioned above, should be firstly considered before further mechanical test or biological test. In order to minimize the geometrical error, more efforts possibly need to be done on processing control like scanning strategy and post surface treatments.

With addition of WE43, porous scaffolds showed the similar tendency of strength and ductility with bulk samples. The elastic modulus of human bones was about 0.4-18 GPa [37]. The ultimate compressive strength and elastic modulus of pure Zn porous scaffolds were 22.9 MPa and 0.95 GPa. Zn-5WE43 porous scaffolds showed the highest strength and relatively high elastic modulus as 73.2 MPa and 2.48 GPa. For comparison, L-PBF produce WE43 porous scaffolds in the same design showed yield strength of 24 MPa and elastic modulus of 0.8 GPa [28]. The elastic modulus of Zn-xWE43 were within the reported value of human bones, which lay a foundation for future clinical applications. The brittle fracture of Zn-5WE43 porous scaffolds indicated low fatigue strength and impact toughness. The angle of fracture plane was 55° to the horizontal plane as shown in Fig. 10. This angle was the same as the angle between the vertical section of the designed diamond lattice and the horizontal plane. It was concluded that the compressive fracture occurred at the position of struts where yellow circle marks indicated in Fig. 2b, which was the tangential plane with the smallest cross section area of struts. Pure Zn and Zn-2WE43 porous scaffolds showed different fracture behavior with a much higher amount of deformation before fracture. The tensile elongation of Zn-2WE43 bulk samples was only 1.8%, but Zn-2WE43 porous scaffolds endured massive plastic deformation before fracture as shown in Fig. 10b. The different fracture behavior between bulk samples and porous scaffolds indicated that the mechanical behavior of porous scaffolds can be greatly adjusted by structural design [37,38]. In the future, further researches on heat treatment and structural design are required for the improvement of mechanical properties.

4. Conclusion

With the mixed powder of pure Zn and WE43 Mg alloy, Zn-xWE43(x = 0, 2, 5 and 8 wt%) porous scaffolds were manufactured by L-PBF process. The formation quality, microstructure and mechanical properties were investigated to address the key technical issues on additive manufacturing of Zn based metal porous scaffolds for biodegradable applications. High densification over 99.47% was achieved for all the used samples under the same processing conditions. Zn-8WE43 showed a bit higher processing porosity, indicating that the optimized processing conditions need to be adjusted according to the content of alloying elements. A large amount of particles adhered to the surface of struts, causing to a big geometrical error between the design shape and L-PBF samples. The designed geometrical porosity reduced from 67% to 45%.

Rapid cooling rate and the addition of WE43 together resulted to very fine grains in L-PBF samples. With increasing the content of WE43, the amount of Zn + Mg $_2$ Zn $_{11}$ eutectics increased, which increased tensile strength but decreased elongation. The formation of brittle MgZn $_2$ deteriorated both strength and elongation. Zn-5WE43 showed the highest tensile strength of 335.4 MPa, but the elongation was only 1%. The compressive strength and Young's modulus of Zn-5WE43 was 73.2 MPa and 2.48 GPa. The fracture behavior of porous scaffolds was directly related to structural design. In the future, more researches are expected on design of Zn alloy powders and geometrical design to promote the real application of additive manufacturing of biodegradable metal porous scaffolds.

Supplementary data to this article can be found online at https://doi.org/10.1016/j.matdes.2019.107937.

Acknowledgement

This work was supported by National Key R&D Program of China (2018YFE0104200) and National Natural Science Foundation of China (51875310).

References

- D. Tang, R.S. Tare, L.Y. Yang, D.F. Williams, K.L. Ou, R.O.C. Oreffo, Biofabrication of bone tissue: approaches, challenges and translation for bone regeneration, Biomaterials 83 (2016) 363–382.
- [2] A.A. Zadpoor, Bone tissue regeneration: the role of scaffold geometry, Biomaterials Science 3 (2) (2015) 231–245.
- [3] H. Shahali, A. Jaggessar, P.K.D.V. Yarlagadda, Recent advances in manufacturing and surface modification of titanium orthopaedic applications, Procedia Engineering 174 (2017) 1067–1076.
- [4] S. Ehtemam-Haghighi, H. Attar, M.S. Dargusch, D. Kent, Microstructure, phase composition and mechanical properties of new, low cost Ti-Mn-Nb alloys for biomedical applications, J Alloy Compd 787 (2019) 570–577.
- [5] S. Ehtemam-Haghighi, K.G. Prashanth, H. Attar, A.K. Chaubey, G.H. Cao, L.C. Zhang, Evaluation of mechanical and wear properties of Ti xNb 7Fe alloys designed for biomedical applications, Mater Design 111 (2016) 592–599.
- [6] A.G. Demir, B. Previtali, Additive manufacturing of cardiovascular CoCr stents by selective laser melting, Mater Design 119 (2017) 338–350.
- [7] D. Kong, X. Ni, C. Dong, L. Zhang, C. Man, X. Cheng, X. Li, Anisotropy in the microstructure and mechanical property for the bulk and porous 316L stainless steel fabricated via selective laser melting, Mater. Lett. 235 (2019) 1–5.
- [8] Y.F. Zheng, X.N. Gu, F. Witte, Biodegradable metals, Mat Sci Eng R 77 (2014) 1–34.
- [9] Y. Liu, Y. Zheng, X.-H. Chen, J.-A. Yang, H. Pan, D. Chen, L. Wang, J. Zhang, D. Zhu, S. Wu, K.W.K. Yeung, R.-C. Zeng, Y. Han, S. Guan, Fundamental theory of biodegradable metals definition, criteria, and design, Adv. Funct. Mater. 0(0) 1805402.
- [10] S. Agarwal, J. Curtin, B. Duffy, S. Jaiswal, Biodegradable magnesium alloys for orthopaedic applications: a review on corrosion, biocompatibility and surface modifications, Mater. Sci. Eng. C Mater. Biol. Appl. 68 (2016) 948–963.

- [11] H. Gong, K. Wang, R. Strich, J.G. Zhou, In vitro biodegradation behavior, mechanical properties, and cytotoxicity of biodegradable Zn–Mg alloy, J Biomed Mater Res B Appl Biomater (2015) n/a–n/a. doi:https://doi.org/10.1002/jbm.b.33341.
- [12] C. Yao, Z. Wang, S.L. Tay, T. Zhu, W. Gao, Effects of mg on microstructure and corrosion properties of Zn-mg alloy, J. Alloys Compd. 602 (2014) 101–107.
- [13] Z. Tang, H. Huang, J. Niu, L. Zhang, H. Zhang, J. Pei, J. Tan, G. Yuan, Design and characterizations of novel biodegradable Zn-Cu-Mg alloys for potential biodegradable implants, Mater. Des. 117 (2017) 84–94.
- [14] E. Mostaed, M. Sikora-Jasinska, J.W. Drelich, M. Vedani, Zinc-based alloys for degradable vascular stent applications, Acta Biomater. 71 (2018) 1–23.
- [15] J. Venezuela, M.S. Dargusch, The influence of alloying and fabrication techniques on the mechanical properties, biodegradability and biocompatibility of zinc: a comprehensive review, Acta Biomater. 87 (2019) 1–40.
- [16] P.K. Bowen, J. Drelich, J. Goldman, Zinc exhibits ideal physiological corrosion behavior for bioabsorbable stents, Adv. Mater. 25 (18) (2013) 2577–2582.
- [17] S. Zhao, J.-M. Seitz, R. Eifler, H.J. Maier, R.J. Guillory II, E.J. Earley, A. Drelich, J. Goldman, J.W. Drelich, Zn-Li alloy after extrusion and drawing: structural, mechanical characterization, and biodegradation in abdominal aorta of rat, Mater. Sci. Eng. C 76 (2017) 301–312.
- [18] M. Montani, A.G. Demir, E. Mostaed, M. Vedani, B. Previtali, Processability of pure Zn and pure Fe by SLM for biodegradable metallic implant manufacturing, Rapid Prototyp. J. 23 (3) (2017) 514–523.
- [19] P. Wen, L. Jauer, M. Voshage, Y. Chen, R. Poprawe, J.H. Schleifenbaum, Densification behavior of pure Zn metal parts produced by selective laser melting for manufacturing biodegradable implants, J Mater Process Tech 258 (2018) 128–137.
- [20] P. Wen, M. Voshage, L. Jauer, Y. Chen, Y. Qin, R. Poprawe, J.H. Schleifenbaum, Laser additive manufacturing of Zn metal parts for biodegradable applications: processing, formation quality and mechanical properties, Mater Design 155 (2018) 36–45.
- [21] Y. Yang, F. Yuan, C. Gao, P. Feng, L. Xue, S. He, C. Shuai, A combined strategy to enhance the properties of Zn by laser rapid solidification and laser alloying, J. Mech. Behav. Biomed. Mater. 82 (2018) 51–60.
- [22] C. Shuai, L. Xue, C. Gao, Y. Yang, S. Peng, Y. Zhang, Selective laser melting of Zn-Ag alloys for bone repair: microstructure, mechanical properties and degradation behaviour, Virtual and Physical Prototyping 13 (3) (2018) 146–154.
- [23] P. Wen, Y. Qin, Y. Chen, M. Voshage, L. Jauer, R. Poprawe, J.H. Schleifenbaum, Laser additive manufacturing of Zn porous scaffolds: shielding gas flow, surface quality and densification, J. Mater. Sci. Technol. 35 (2) (2019) 368–376.
- [24] Y. Qin, P. Wen, H. Guo, D. Xia, Y. Zheng, L. Jauer, R. Poprawe, M. Voshage, J.H. Schleifenbaum, Additive manufacturing of biodegradable metals: current research status and future perspectives, Acta Biomater. (2019)https://doi.org/10.1016/j.actbio.2019.04.046.
- [25] M. Haude, R. Erbel, P. Erne, S. Verheye, H. Degen, D. Böse, P. Vermeersch, I. Wijnbergen, N. Weissman, F. Prati, R. Waksman, J. Koolen, Safety and performance of the drug-eluting absorbable metal scaffold (DREAMS) in patients with de-novo coronary lesions: 12 month results of the prospective, multicentre, first-in-man BIOSOLVE-I trial, Lancet 381 (9869) (2013) 836–844.

- [26] N.A. Zumdick, L. Jauer, L.C. Kersting, T.N. Kutz, J.H. Schleifenbaum, D. Zander, Additive manufactured WE43 magnesium: a comparative study of the microstructure and mechanical properties with those of powder extruded and as-cast WE43, Mater. Charact. 147 (2019) 384–397.
- [27] H. Attar, M. Calin, L.C. Zhang, S. Scudino, J. Eckert, Manufacture by selective laser melting and mechanical behavior of commercially pure titanium, Mat Sci Eng A 593 (2014) 170–177.
- [28] Y. Li, J. Zhou, P. Pavanram, M.A. Leeflang, L.I. Fockaert, B. Pouran, N. Tumer, K.U. Schroder, J.M.C. Mol, H. Weinans, H. Jahr, A.A. Zadpoor, Additively manufactured biodegradable porous magnesium, Acta Biomater. 67 (2018) 378–392.
- [29] A.B. Spierings, M. Schneider, R. Eggenberger, Comparison of density measurement techniques for additive manufactured metallic parts, Rapid Prototyp. J. 17 (2011) 380–386.
- [30] T. Prosek, A. Nazarov, U. Bexell, D. Thierry, J. Serak, Corrosion mechanism of model zinc-magnesium alloys in atmospheric conditions, Corros. Sci. 50 (8) (2008) 2216-2231.
- [31] K. Wei, Z. Wang, X. Zeng, Influence of element vaporization on formability, composition, microstructure, and mechanical performance of the selective laser melted Mg–Zn–Zr components, Mater. Lett. 156 (2015) 187–190.
- [32] C. Emmelmann, D. Herzog, J. Kranz, 10 design for laser additive manufacturing, in: M. Brandt (Ed.), Laser Additive Manufacturing, Woodhead Publishing 2017, pp. 259–279.
- [33] D. Vojtech, J. Kubasek, J. serak, P. Novak, Mechanical and corrosion properties of newly developed biodegradable Zn-based alloys for bone fixation, Acta Biomater. 7 (2011) 3515–3522.
- [34] E. Mostaed, M. Sikora-Jasinska, A. Mostaed, S. Loffredo, A.G. Demir, B. Previtali, D. Mantovani, R. Beanland, M. Vedani, Novel Zn-based alloys for biodegradable stent applications: design, development and in vitro degradation, J. Mech. Behav. Biomed. Mater. 60 (2016) 581–602.
- [35] P. Minárik, J. Veselý, J. Čížek, M. Zemková, T. Vlasák, T. Krajňák, J. Kubásek, R. Král, D. Hofman, J. Stráská, Effect of secondary phase particles on thermal stability of ultrafine grained Mg-4Y-3RE alloy prepared by equal channel angular pressing, Mater. Charact. 140 (2018) 207–216.
- [36] T. DebRoy, H.L. Wei, J.S. Zuback, T. Mukherjee, J.W. Elmer, J.O. Milewski, A.M. Beese, A. Wilson-Heid, A. De, W. Zhang, Additive manufacturing of metallic components – process, structure and properties, Prog. Mater. Sci. 92 (2018) 112–224.
- [37] X. Wang, S. Xu, S. Zhou, W. Xu, M. Leary, P. Choong, M. Qian, M. Brandt, Y.M. Xie, To-pological design and additive manufacturing of porous metals for bone scaffolds and orthopaedic implants: a review, Biomaterials 83 (2016) 127–141.
- [38] F.S. Bobbert, K. Lietaert, A.A. Eftekhari, B. Pouran, S.M. Ahmadi, H. Weinans, A.A. Zadpoor, Additively manufactured metallic porous biomaterials based on minimal surfaces: a unique combination of topological, mechanical, and mass transport properties, Acta Biomater. 53 (2017) 572–584.